Neuron. Author manuscript; available in PMC 2016 December 08.

Published in final edited form as:

Neuron. 2010 July 15; 67(1): 100–115. doi:10.1016/j.neuron.2010.06.003.

Septins Regulate Developmental Switching from Microdomain to Nanodomain Coupling of Ca^{2+} Influx to Neurotransmitter Release at a Central Synapse

Yi-Mei Yang[1,2,6], **Michael J. Fedchyshyn**[1,2,6], **Giovanbattista Grande**[1,2], **Jamila Aitoubah**[1,2], **Christopher W. Tsang**[3,4], **Hong Xie**[3,4], **Cameron A. Ackerley**[5], **William S. Trimble**[3,4,*], and **Lu-Yang Wang**[1,2,*]

[1]Program in Neurosciences and Mental Health, The Hospital for Sick Children, Toronto, M5G 1X8 ON, Canada

[2]Department of Physiology, University of Toronto, Toronto, M5S 1A8 ON, Canada

[3]Program in Cell Biology, The Hospital for Sick Children, Toronto, M5G 1X8 ON, Canada

[4]Department of Biochemistry, University of Toronto, Toronto, M5S 1A8 ON, Canada

[5]Department of Paediatric Laboratory Medicine, The Hospital for Sick Children, Toronto, M5G 1X8 ON, Canada

SUMMARY

Neurotransmitter release depends critically on close spatial coupling of Ca^{2+} entry to synaptic vesicles at the nerve terminal; however, the molecular substrates determining their physical proximity are unknown. Using the calyx of Held synapse, where “microdomain” coupling predominates at immature stages and developmentally switches to “nanodomain” coupling, we demonstrate that deletion of the filamentous protein Septin 5 imparts immature synapses with striking morphological and functional features reminiscent of mature synapses. This includes synaptic vesicles tightly localized to active zones, resistance to the slow Ca^{2+} buffer EGTA and a reduced number of Ca^{2+} channels required to trigger single fusion events. Disrupting Septin 5 organization acutely transforms microdomain to nanodomain coupling and potentiates quantal output in immature wild-type terminals. These observations suggest that Septin 5 is a core molecular substrate that differentiates distinct release modalities at the central synapse.

INTRODUCTION

Septins, a conserved family of GTP/GDP-binding proteins encoded by 14 genes in mammals, are filamentous proteins associated with a variety of biological processes including secretion, phagocytosis, cytokinesis, sperm motility, and neurological diseases such as Parkinson’s and schizophrenia (Ihara et al., 2003; Barral and Kinoshita, 2008; Weirich et al., 2008; Suzuki et al., 2009). Although septins are required for cell division in organisms as diverse as yeast and humans, many of them are abundantly expressed in

*Correspondence: w.trimble@utoronto.ca (W.S.T.), luyang.wang@utoronto.ca (L.-Y.W.).

[6]These authors contributed equally to this work

postmitotic neurons (Hsu et al., 1998; Walikonis et al., 2000; Tada et al., 2007; Xie et al., 2007; Tsang et al., 2008), where their functions remain largely unknown. Ultrastructural studies of central synapses have shown that synaptic vesicles (SVs) in proximity to the presynaptic membrane are encircled by a mesh of filaments emanating from the active zone (AZ) (Hirokawa et al., 1989; Dresbach et al., 2001; Schoch and Gundelfinger, 2006; Siksou et al., 2007). This implicates a potential role of these filaments in docking or positional priming of SVs to the AZ before fusion takes place (Hirokawa et al., 1989; Beites et al., 2005). Septins from the rat brain form filaments with a diameter of 8.25 nm and lengths that are multiples of 25 nm (Hsu et al., 1998), approximately the same sizes as the filaments observed by electron microscopy at the AZ (Hirokawa et al., 1989; Siksou et al., 2007). In secretory cells, septin 5 (Sept5) or Sept5 containing filaments bind to syntaxin and appear to act as a molecular “brake” preventing vesicle association with the t-SNARE complex, thereby inhibiting release (Beites et al., 1999, 2005). Thus septins, and Sept5 in particular, are intriguing candidates as part of the filamentous mesh surrounding SVs in the nerve terminal.

One possible function of these filaments is that they establish the distance between SVs and AZs in central synapses and in doing so, affect the spatiotemporal coupling of SVs to incoming calcium transients via voltage-gated Ca^{2+} channels (VGCCs). Work in nonmammalian synapses indicates that VGCCs are tightly coupled to the release sites where SVs are docked such that release of a single SV requires activation of as few as one VGCC (i.e., nanodomain model) (Yoshikami et al., 1989; Augustine, 1990; Roberts et al., 1990; Stanley, 1991). However, in mammalian central synapses, a larger number of VGCCs with varying subtypes are often engaged in a cooperative manner to trigger single fusion events (i.e., microdomain model) (Wu and Saggau, 1994; Mintz et al., 1995; Borst et al., 1995; Sabatini and Regehr, 1997; Wu et al., 1998; Geiger and Jonas, 2000). Unfortunately, evidence in support of each model has been generated from functionally distinct synapses with up to 10-fold differences in extracellular Ca^{2+} concentration ($[Ca^{2+}]_e$), fuelling an intensive debate on how VGCCs and SVs are coupled (Meinrenken et al., 2003; Gentile and Stanley, 2005; Neher and Sakaba, 2008).

We have previously demonstrated that the coupling of VGCCs to SVs at the calyx of Held, a giant excitatory glutamatergic synapse in the auditory brainstem, undergoes a developmental transformation from a “microdomain” to “nanodomain” modality (Fedchyshyn and Wang, 2005). The nanodomain coupling also operates at the hippocampal basket cell-granule cell inhibitory synapses (Bucurenciu et al., 2008). These observations from both excitatory and inhibitory synapses lead us to hypothesize that microdomain and nanodomain coupling modalities are distinct physical entities and that the spatial proximity of VGCCs and SVs is highly regulated, possibly via presynaptic cytomatrix filaments such as septins. Taking advantage of the coexistence of microdomain and nanodomain coupling modalities and their developmental switch at the mouse calyx of Held synapse, we investigate potential roles of Sept5 in regulating the subsynaptic reorganization of AZ elements and its functional consequences on quantal output. Our results indicate that Sept5 is of critical importance for modulating the positional proximity between SVs and AZs and the input-output relationship of the synapse.

RESULTS

Distinct Patterns of Sept5 in the Developing Calyx of Held Synapse

Within the first 3 postnatal (P) weeks, the calyx of Held synapse develops rapidly in both its functionality and morphology. From synapse formation around P1–3 to the opening of the ear canal (i.e., external sound stimuli) at P11/12 and to final maturation beyond P14, profound adaptations in the biophysical properties of pre- and postsynaptic elements converge to facilitate the development of high-fidelity transmission at extraordinarily high rates (>600 Hz) (Trussell, 1997; von Gersdorff and Borst, 2002). In parallel, calyces transform morphologically from a spoon/club-like structure with thin filopodia to a highly digitated structure with stalks and swellings containing a total of 500–800 AZs (Rollenhagen and Lübke, 2006; Wimmer et al., 2006). These structural transformations are important for supporting release and replenishment of SVs, facilitating clearance of neurotransmitter and alleviating postsynaptic desensitization during high-frequency transmission (Wang and Kaczmarek, 1998; Joshi and Wang, 2002; Taschenberger et al., 2002; Schneggenburger and Forsythe, 2006). To investigate whether Sept5 is expressed in the developing calyx of Held synapse, we used specific antibodies against the presynaptic marker vesicular glutamate transporter 1 (vGLUT1) and Sept5 to label developing calyx of Held terminals in auditory brainstem slices taken from P8–12 (immature) and P16–19 (mature) wild-type (*Sept5*$^{+/+}$) and Sept5 knockout (*Sept5*$^{-/-}$) mice. Both vGLUT1 and Sept5 antibodies showed strong colabeling in presynaptic calyces but not in postsynaptic principal neurons in the medial nucleus of the trapezoid body (MNTB) (Figures 1A–1D), indicating that Sept5 proteins are primarily expressed in nerve terminals. In contrast, no Sept5 labeling was observed in presynaptic calyces from *Sept5*$^{-/-}$ mice, demonstrating high specificity of the Sept5 antibody (Figure 1E). In immature calyces, vGLUT1 staining formed continuous rings consistent with a homogenous distribution of SVs within the spoon-like structured calyx of Held terminal (Figures 1A–1C). In these synapses, Sept5 staining exhibited a high degree of overlap with vGLUT1 (see colocalization plot, Figures 1Bb1–1Bb3) but appeared as clusters near the release face of the calyx as indicated by the intermittent peaks in the line intensity plots in Figures 1B and 1C, right panels). In contrast, vGLUT1 and Sept5 staining in mature calyces were more punctate with minimal overlap as evidenced by an obvious lack of blending of the red and green fluorophores (Figures 1Bb4–1Bb6; also see colocalization plot, right bottom panels) and their out-of-phase localization with line scans along the calyceal release face (Figure 1D). These observations suggest that Sept5 filaments are present in the nerve terminal but undergo a developmental reorganization.

Engagement of Sept5 in Developmental Reorganization of SVs Near AZs

To more closely examine the spatial relationship between Sept5 and SVs in the developing calyx of Held synapse, we constructed three-dimensional images of a sample portion of the calyx terminal (Figures 2Aa1, 2Aa2, 2Bb1, and 2Bb2). When image stacks were rotated, strong overlap of vGLUT1 and Sept5 labeling was observed on the release face of the calyx terminal (Figure 2Aa3) compared to the opposing side (Figure 2Aa4). In contrast, vGLUT1 and Sept5 in the mature calyx appeared anatomically segregated regardless of the plane in which the image stack was viewed (Figure 2B). This raises the possibility that both Sept5 and SVs are tethered near the release sites in immature terminals but spatially reorganize

such that they occupy distinct subsynaptic regions within the calyx terminal at maturity. To address this more directly, we stained the MNTB for vGLUT1 and the AZ marker Bassoon and found that similar to the Sept5 staining, Bassoon labeling, which appeared punctate, was highly colocalized with vGLUT1 in immature calyx terminals as indicated by the line intensity scans in Figure 2C. However, in mature calyces, unlike the case for Sept5 (Figure 1D), Bassoon and vGLUT1 were also highly colocalized within the calyx terminal (Figure 2D), suggesting Sept5 filaments are depleted from the AZ following development.

Given this apparent developmental difference in the Sept5 distribution patterns, we hypothesized that this filamentous protein may play a role in subsynaptic organization of SVs near AZs. To test this, we performed transmission electron microscopy (tEM) on brainstem slices containing the MNTB from *Sept5*$^{+/+}$ and *Sept5*$^{-/-}$ mice at P8–12 and P16–19. Upon initial inspection of tEM images from *Sept5*$^{+/+}$ calyces, we found that a greater number of SVs appeared to be in physical contact with the AZ membrane in mature synapses (Figures 2Ff1 and 2Ff2) compared to immature synapses (Figures 2Ee1 and 2Ee2). To quantify this observation, we measured separation distances between the closest edge of the SVs and AZs in immature and mature synapses up to 100 nm of vertical depth away from each AZ and constructed normalized histograms for both age groups. In mature synapses, nearly 22% of SVs were found to be docked within the first 5 nm from the AZ, compared to only 10.5% in immature synapses (total SVs = 1694 for P16–18 versus 1678 for P8–12, n = 6 versus 6 calyces; Figure 2G). However, in immature synapses there was a greater proportion of SVs positioned between 5 and 20 nm from the AZ compared to mature synapses (~10% versus 5.5%). Beyond 20 nm from the AZ, the distribution of SVs was similar in both age groups. Overall, when plotted as a cumulative histogram, the distribution of SVs within 100 nm of the AZ was significantly different between immature and mature synapses (Kolmogorov-Smirnov [K-S] test, $p < 0.01$). Surprisingly, in *Sept5*$^{-/-}$ synapses SVs within 100 nm of the AZ were similarly distributed at both age groups (K-S test; $p > 0.05$ for overall distribution; Figure 2H). Importantly, in immature *Sept5*$^{-/-}$ synapses, there was an increase in the number of SVs within 5 nm of the AZ compared to the age-matched *Sept5*$^{+/+}$ controls (17% versus 10.5%). Furthermore, the overall distribution of SVs within 100 nm of the AZ was not significantly different between immature *Sept5*$^{-/-}$ synapses and mature *Sept5*$^{+/+}$ synapses (K-S test, $p > 0.05$). In immature synapses, the number of SVs within 5nmper AZ was dramatically increased by deletion of Sept5 from 0.83 ± 0.07 (n = 220 AZs) to 2.44 ± 0.14 (n = 117 AZs) ($p < 0.05$) (Figure 2I). The former number is substantially lower than that previously reported for the rat calyx of Held synapse (~6 and 3 SVs/AZ at P5 and P14, respectively (Taschenberger et al., 2002)), which may be accounted for by differences in analysis and/or two species which in fact have different developmental profiles of synaptic strength (Taschenberger and von Gersdorff, 2000; Iwasaki and Takahashi, 2001; Joshi and Wang, 2002). However, knockout of Sept5 did not affect the number of closely docked SVs at mature synapses (2.17 ± 0.13, n = 185 AZs, for *Sept5*$^{+/+}$ versus 2.49 ± 0.15, n = 157 AZs, for *Sept5*$^{-/-}$; Figure 2I). Collectively, these observations suggest that Sept5 filaments preferentially target release sites facing the synaptic cleft in immature synapses, but locates in between release sites in mature synapses. This reorganization may allow a larger proportion of nearby SVs to become more closely docked to the AZ. Thus, Sept5 or Sept5 containing filaments appear to act as a spatial barrier

separating SVs from docking tightly to AZs in immature synapses, deletion of which leads to an increase in the number of docked SVs, reminiscent of the subsynaptic arrangement observed in mature calyces.

Deletion of Sept5 Increases Quantal Output and the Readily Releasable Pool (RRP)

Given the morphological finding that Sept5 plays a role in the subsynaptic positioning of SVs near AZs, we investigated the functional properties of the calyx of Held synapse in both immature and mature *Sept5*$^{+/+}$ and *Sept5*$^{-/-}$ mice using single and paired patch-clamp recording techniques. We found that evoked excitatory postsynaptic currents (EPSCs or I_{EPSC}) from immature synapses were significantly larger in *Sept5*$^{-/-}$ than in *Sept5*$^{+/+}$ synapses (P8–12: 7.6 ± 0.3 versus 6.4 ± 0.3 nA, n = 15 versus 14; $p < 0.05$; $[Ca^{2+}]_e$ = 2 mM). Mature synapses showed marked increases in I_{EPSC}, but no significant difference was observed between *Sept5*$^{-/-}$ and *Sept5*$^{+/+}$ synapses (P16–18: 13.7 ± 0.8 versus 12.2 ± 0.7 nA, n = 7 versus 8; $p > 0.05$; $[Ca^{2+}]_e$ = 2 mM; Figures 3A and 3B), indicating that a loss of Sept5 selectively potentiates vesicular release from immature synapses but not mature ones. This potentiation was further confirmed by experiments in which we performed simultaneously paired voltage-clamp recordings from pre- and postsynaptic elements of the calyx of Held synapses in immature and mature *Sept5*$^{+/+}$ and *Sept5*$^{-/-}$ mice. We used an action potential waveform (previously recorded from an immature P10 calyx) as a voltage-command template (AP_I) to evoke presynaptic calcium currents (I_{Ca}) and the resulting I_{EPSC} from both immature and mature synapses in lower $[Ca^{2+}]_e$ (i.e., 1 mM) so as to reduce voltage-clamp errors and postsynaptic desensitization. With such paradigms, we again found a significant increase in I_{EPSC} in immature *Sept5*$^{-/-}$ over *Sept5*$^{+/+}$ synapses (P8–12: 3.2 ± 0.2 versus 2.0 ± 0.3 nA, n = 6 versus 7; $p < 0.05$; Figures 3C and 3D), while presynaptic I_{Ca} remained indistinguishable in shape and size. In contrast, no difference in I_{EPSC} was detected between the two groups of mature synapses (P16–18: 15.9 ± 0.6 versus 14.9 ± 0.7 nA, n = 6 versus 6; $p > 0.05$; Figures 3C and 3D). We measured synaptic delay (SD) with the maximal curvature method (Fedchyshyn and Wang, 2007) and observed a selective decrease at immature *Sept5*$^{-/-}$ synapses compared to that at immature *Sept5*$^{+/+}$ synapses (0.3 ± 0.02 versus 0.38 ± 0.02 ms, n = 6 versus 7; $p < 0.05$; Figures 3C and 3E), and such a difference in SD was absent in mature synapses (0.16 ± 0.01 versus 0.17 ± 0.01ms, n = 6 versus 6; $p > 0.05$). These results suggest that the increase in quantal output in immature *Sept5*$^{-/-}$ synapses is independent of variability in AP waveform and I_{Ca}, and that removal of Sept5 accelerates the temporal onset of transmitter release.

With morphological evidence showing more docked SVs at AZs in immature *Sept5*$^{-/-}$ synapses, we next asked whether the loss of Sept5 alters the size of RRP and its depletion and recovery. We stimulated afferent axons with two high-frequency trains (i.e., 100 Hz, 200 ms, $[Ca^{2+}]_e$ = 2mM) separated by different time intervals (Δt), with the first train to induce short-term depression (STD) which mainly reflects depletion of SVs in the RRP, and the second train to measure replenishment of RRP (Figure 3F; Wang and Kaczmarek, 1998; Taschenberger et al., 2002; Schneggenburger et al., 2002). The current densities from each I_{EPSC} in the first trains were summated to generate cumulative plots (Figure 3G), from which the RRP current densities were back-extrapolated using linear regression of the steady-state I_{EPSC} for both *Sept5*$^{+/+}$ and *Sept5*$^{-/-}$ synapses (Schneggenburger et al., 1999).

Immature *Sept5*$^{+/+}$ and *Sept5*$^{-/-}$ synapses had the RRP current integral of 16.3 ± 0.3 and 22.6 ± 0.1 pC (coulombs) (n = 14 and 15, $p < 0.01$, $[Ca^{2+}]_e$ = 2 mM; Figure 3G) respectively, in line with the notion that morphologically docked SVs are likely the physiological correlate of the RRP, and therefore more docked SVs in *Sept5*$^{-/-}$ synapses yield a greater RRP. In contrast, the time course and extent of STD and the recovery of RRP were comparable between *Sept5*$^{+/+}$ and *Sept5*$^{-/-}$ synapses (Figures 3H and 3I). Furthermore, spontaneous miniature EPSCs (mEPSCs) recorded from immature *Sept5*$^{+/+}$ and *Sept5*$^{-/-}$ synapses showed no significant difference in either frequency (0.9 ± 0.1 versus 0.7 ± 0.1 Hz, $p > 0.05$) or amplitude (46 ± 1 pA versus 48 ± 2 pA, $p > 0.05$, n = 17 versus 16; Figures 3J–3L). These results suggest that Sept5 may function to establish a physical barrier preventing SVs from readily docking; therefore, deletion of Sept5 results in an expanded RRP by allowing more docked SVs at AZs. As a consequence, action potential evoked release increases, independent of any changes in unitary quantal properties.

Nanodomain Coupling in Immature *Sept5*$^{-/-}$ Synapses

If Sept5 indeed acts in immature synapses to prevent close association of SVs with AZs, where VGCCs reside, deletion of Sept5 should also result in a tighter coupling of Ca^{2+} influx to vesicular release. To test this, we examined the input-output relationships of *Sept5*$^{+/+}$ and *Sept5*$^{-/-}$ synapses by performing paired voltage-clamp recordings of presynaptic I_{Ca} and postsynaptic I_{EPSC}. The input-output relationship at any given synapse can be well described by a power function in the form of $I_{EPSC} \propto [I_{Ca}]^m$, where m denotes the Ca^{2+} cooperativity (Matveev et al., 2009). When specific presynaptic voltage paradigms (i.e., voltage ramps from −80 mV to +60 mV with 0.1 ms increments in plateau duration, $[Ca^{2+}]_e$ = 1 mM; Figure 4A) are used, an increasing number of VGCCs can be recruited. Because such voltage steps maximize the open probability of VGCCs while the driving force for Ca^{2+} remains the same for all open channels (Augustine et al., 1987; Borst and Sakmann, 1998, 1999; Gentile and Stanley, 2005; Fedchyshyn and Wang, 2005), the only variable at any given plateau duration is then the number of VGCCs engaged in mediating release of SVs. The m value obtained with such paradigms, known as "Ca^{2+} channel/domain cooperativity," therefore allows direct inference into the required number of Ca^{2+} channels for gating single fusion events. Figure 4A shows two sets of recordings from immature *Sept5*$^{+/+}$ and *Sept5*$^{-/-}$ synapses, in which progressive increases in I_{Ca} led to nonlinear increases in I_{EPSC}. When the integrated areas of I_{Ca} and I_{EPSC} in each synapse were normalized and graphed on double logarithmic coordinates (Figure 4B), we could readily derive m from the slope of linear fits to the data sets. We found that m values for *Sept5*$^{-/-}$ synapses were significantly reduced compared to *Sept5*$^{+/+}$ synapses (P8–12: 3.3 ± 0.1 versus 5.0 ± 0.4, $p < 0.01$, n = 7 versus 9; Figure 4C), indicating that the number of Ca^{2+} channels engaged in release of single SVs is reduced in immature *Sept5*$^{-/-}$ synapses. In contrast, tightly coupled mature *Sept5*$^{+/+}$ and *Sept5*$^{-/-}$ synapses showed no significant change in m values upon deletion of the Sept5 protein (2.7 ± 0.1 versus 3.0 ± 0.2, n = 6 versus 6, $p > 0.05$; Figure 4C). In fact, the m value for immature *Sept5*$^{-/-}$ synapses (3.3) approaches that observed in mature synapses. This suggests that deletion of Sept5 from immature synapses decreases the cooperative requirements for Ca^{2+}-domain overlap in releasing SVs, inducing a functional coupling modality which would otherwise take more than 2 postnatal weeks to evolve during development.

Previous work has demonstrated that the spatial coupling between VGCCs and SVs tightens while the sensitivity of Ca^{2+} sensors on SVs remains unchanged or slightly decreased during development (Fedchyshyn and Wang, 2005; Yang and Wang, 2006; Wang et al., 2008; Kochubey et al., 2009). As a result, the subsynaptic transformation from microdomain to nanodomain modality significantly boosts quantal output during an action potential. Immature *Sept5*$^{-/-}$ synapses appear to manifest some of the distinct morphological and functional characteristics observed in mature *Sept5*$^{+/+}$. To directly probe the nature of spatial coupling between VGCCs and SVs in immature *Sept5*$^{-/-}$ synapses, we made use of the Ca^{2+} buffer EGTA. Because EGTA has a slow forward-rate constant for binding Ca^{2+}, it is expected that EGTA will effectively intercept Ca^{2+} ions in transit and attenuate transmitter release only when VGCCs and SVs are physically distant (i.e., microdomain) but will be ineffective in sequestering Ca^{2+} if they are so tightly tethered that Ca^{2+} reaches the sensors before being captured by EGTA (i.e., nanodomain) (Adler et al., 1991; Borst et al., 1995; Naraghi and Neher, 1997; Meinrenken et al., 2002; Fedchyshyn and Wang, 2005; Bucurenciu et al., 2008; Leão and von Gersdorff, 2009). We first recorded axonally evoked EPSCs while a patch electrode containing EGTA (10 mM) was sealed onto the presynaptic calyx in cell-attached mode (Figure 4D). Following measurement of control EPSCs, the presynaptic membrane was ruptured to allow EGTA diffusion and equilibration between the patch pipette and the calyx for ~3 min. After equilibration, paired recordings of presynaptic action potentials in current-clamp mode and EPSCs were performed to measure the impact of EGTA on SV release. Injection of 10 mM EGTA into immature presynaptic terminals potently attenuated I_{EPSC} in *Sept5*$^{+/+}$ synapses, whereas *Sept5*$^{-/-}$ synapses showed little sensitivity to the same manipulation (54.0% ± 2.7% versus 14.1% ± 4.4%, n = 5 versus 5, $p < 0.01$; Figures 4E–4G). Furthermore, the waveform of action potentials in *Sept5*$^{+/+}$ and *Sept5*$^{-/-}$ synapses remained identical (amplitude: 118.3 ± 2.2 mV versus 122.8 ± 1.6 mV, $p > 0.05$; halfwidth: 0.41 ± 0.02 ms 0.42 ± 0.02 ms, n = 12 versus 10, $p > 0.05$; Figure 4H). These observations, along with the morphological and functional evidence, collectively demonstrate that independent of presynaptic excitability, deletion of Sept5 specifically imparts immature synapses with phenotypic features of the nanodomain coupling modality typical of mature synapses.

Disruption of Sept5 Filaments in AZs Acutely Transforms Microdomain to Nanodomain Coupling Modality

Our results from immature *Sept5*$^{-/-}$ synapses implicate Sept5 as a potential candidate involved in gating microdomain and nanodomain coupling modalities at the developing calyx of Held synapse. However, it is possible that the apparent morphological and functional phenotypes arising in *Sept5*$^{-/-}$ synapses may stem from compensational mechanisms that simply accelerate maturation in knockout mice. Knowing that microdomain coupling predominates in immature wild-type synapses, we postulated that disruption of endogenous Sept5 filaments would acutely transform microdomain to nanodomain modality. To test this idea, we sought reagents that specifically target Sept5 filaments but not other filaments. We first overexpressed Sept5 or actin filaments tagged with green fluorescence protein (Sept5-GFP or actin-GFP) in Chinese hamster ovary (CHO) cells and imaged their profiles with high-resolution confocal microscopy. Sept5 filaments were widely distributed throughout the cytoplasm, outside the nucleus of transfected cells,

and could be observed as short and curled filaments (Figure 5A, top panel). In contrast, actin-GFP filaments appeared to be much longer and straight in shape (Figure 5B, top panel). To test whether we could disrupt normal distribution patterns of Sept5 filaments, we performed simultaneous imaging and patch-clamp experiments in which recording pipettes were filled with intracellular solution containing SP20, a Sept5 monoclonal antibody, ranging from 1:200 to 1:2000 dilutions. Anti-septin antibodies have previously been shown to block the functions of septins in cells (Surka et al., 2002). As illustrated by real-time images in Figure 5A, we found that ordered structures of Sept5-GFP filaments began to disassemble and form small puncta within the first minute after membrane rupture via the patch electrode (1:200 dilution of SP20). The puncta appeared as bright fluorescent spots which increased drastically over 2 min after SP20 injection. As the antibody solution fully diffused into the recorded cell, Sept5 filaments completely disappeared by 5 min. These striking images represent the first direct evidence that ordered septin filaments can be acutely disrupted by such a manipulation. In contrast, injection of SP20 at the same concentrations into CHO cells expressing actin-GFP filaments had no effect on their structure and distribution patterns (Figure 5B), demonstrating that SP20 is a specific and potent functional blocker for Sept5 filaments.

After establishing the role of SP20 in breaking down Sept5 filaments in CHO cells, we next examined its effects on native central nerve terminals by directly injecting it into presynaptic calyces using the same paradigms as describe above for EGTA experiments. To avoid nonspecific effects of SP20, we employed SP20 at its minimal effective concentration (1:2000 dilution). Upon dialyzing calyces for five minutes, we found SP20 significantly enhanced I_{EPSC} in immature *Sept5*$^{+/+}$ synapses but had no effect in *Sept5*$^{-/-}$ synapses (40.3% ± 7.9% versus 1.0% ± 3.5%; n = 6 versus 6; $p < 0.01$; Figures 6A–6C). Similarly, injection of the BD3 domain peptide of the CDC42 effector protein Borg3, which is known to disrupt the organization of septin filaments (Joberty et al., 2001; Sheffield et al., 2003), also significantly increased I_{EPSC} in immature *Sept5*$^{+/+}$ synapses but was much less effective in potentiating I_{EPSC} in *Sept5*$^{-/-}$ synapses (40.3% ± 7.2% versus 13.0% ± 8.5%; n = 6 versus 5, $p < 0.05$; Figure 6D). Control experiments performed with the same vehicle solution devoid of antibodies (preabsorbed with protein G) or peptide also had little effect on I_{EPSC} amplitude in *Sept5*$^{+/+}$ synapses (data not shown), indicating that SP20 and Borg3 peptide enhance transmitter release by disrupting Sept5 filaments. We next measured Ca^{2+} channel/domain cooperativity (*m* values) in immature *Sept5*$^{+/+}$ synapses preloaded with control and SP20 solutions for 5 min (Figures 6E and 6F). In these synapses, we found that SP20 significantly reduced *m* values to those observed in mature synapses (control: 5.6 ± 0.3 versus SP20: 3.5 ± 0.1, n = 6 versus7, $p < 0.01$; Figures 6G and 6H).

When the same antibody was used to perform immunogold EM experiments in ultrathin frozen sections without osmium tetroxide postfixation to preserve the antigenic epitope (Figure 7A), we found extensive labeling of presynaptic membranes and SVs in immature calyces, which sharply contrasted the sparse labeling in mature calyces. Quantitative analyses of gold particles along the cytoplasmic membrane near any given AZ (0.5 μm from the AZ center) revealed a significant downregulation in the particle density from 12.2 ± 0.6 at P10 to 4.9 ± 0.4 particles/μm at P17 ($p < 0.01$) (Figure 7B). More importantly, the particles in immature synapses were associated with both the AZ and peri-AZ membranes,

whereas in mature synapses the particles were largely located in peri-AZ membranes. This is illustrated in the spatial distribution probability plots in Figure 7C showing significant differences within 0.3 μm of the AZ center but similar incremental gradients away from the AZ center. Taken together, these subsynaptic morphological and functional data indicate that Sept5 filaments are closely associated with AZs in immature synapses, and acute disruption of these filaments readily converts the coupling modality in immature synapses to that in mature synapses, independent of other compensatory developmental mechanisms.

DISCUSSION

Septins are an enigmatic family of GTPase proteins that form ordered complexes important for cell division and architecture (Barral and Kinoshita, 2008; Weirich et al., 2008). Our study revealed surprising effects of these proteins in postmitotic neurons, more specifically in regulating the spatiotemporal control of transmitter release. We demonstrated that Sept5 filaments preferentially localize to the release face of the immature calyx of Held synapse but segregate to the periphery of AZs appearing between clusters of SVs in mature terminals (Figures 1, 2, and 7). In the context of the EM evidence showing distinct patterns of docked SVs and Sept5 filaments in immature and mature synapses and their functional correlates (i.e., I_{EPSC} and RRP) (Figures 2 and 3), we suggest that Sept5 plays diverse roles in the subsynaptic reorganization of release elements during development with little effects on presynaptic action potential waveform and I_{Ca} (Figures 3 and 4). With immature *Sept5*$^{-/-}$ synapses recapitulating major functional features of mature *Sept5*$^{+/+}$ synapses (i.e., low *m* and EGTA insensitivity), it is tempting to speculate that developing immature synapses may use Sept5 filaments as a spatial barrier (Figure 7D), preventing overexcitation and preserving the RRP for action potential-evoked release. As more release sites differentiate and the RRP expands during maturation, Sept5 is depleted from the AZs through yet to be identified mechanisms, such that SVs are more tightly docked onto AZs to ultimately enhance quantal output and shorten temporal delays of transmitter release (Figure 7E). At maturity, Sept5 may instead serve to physically compartmentalize individual AZs by forming diffusion barriers in the peri-AZ regions. Depletion of Sept5 filaments from immature synapses may allow more docked SVs and shorten the physical distance between VGCCs and SVs vertically and/or laterally but have little effects on mature synapses (Figures 7F and 7G).

Different from classical work in non-mammalian synapses where as few as one VGCC gates single fusion events (i.e., nanodomain modality) (Yoshikami et al., 1989; Augustine, 1990; Stanley, 1991), previous studies in mammalians show that many central synapses require the cooperative action of multiple numbers and subtypes of VGCCs to trigger neurotransmitter release (i.e., microdomain modality) (Wu and Saggau, 1994; Mintz et al., 1995; Borst et al., 1995; Sabatini and Regehr, 1997; Wu et al., 1998; Geiger and Jonas, 2000). However, emerging evidence suggests that nanodomain coupling modality exists in both excitatory and inhibitory central synapses (Fedchyshyn and Wang, 2005; Bucurenciu et al., 2008). Our previous work at the mouse calyx of Held synapse has revealed a developmental transformation from microdomain modality in immature synapses to nanodomain modality in mature synapses, which underlies the leftward shift in the input-output relationship of Ca^{2+}-dependent vesicular release (Fedchyshyn and Wang, 2005; Yang and Wang, 2006). As a result of tightened coupling between VGCCs and SVs, the local peak Ca^{2+} concentration

seen by Ca^{2+} sensors on SVs significantly increases from 35 to 56 μM and the release rate increases from ~600 SVs/ms to 1000 SVs/ms despite smaller and briefer Ca^{2+} transient due to developmental action potential narrowing (Wang et al., 2008), as has also been shown for the developing rat calyx of Held synapse (Kochubey et al., 2009). With a different topographic arrangements of VGCCs and SVs from previous modeling work for immature calyces (Meinrenken et al., 2002), we have recently performed computer simulations to conceptualize our findings with a theoretic model, in which we assumed a ring of VGCCs are positioned with equal distance from single SVs (Wang et al., 2009). Our experimental data from developing calyx of Held synapses can be well recapitulated by tightening the coupling between VGCCs and SVs. In immature synapses, microdomain modality operates with cooperative action of 5~6 VGCCs positioned approximately 61 nm away from a SV to trigger single fusion events, while nanodomain modality in mature synapses engages openings of only 2~3 VGCCs placed at 23 nm from a SV to mediate its fusion with the AZ during an action potential (Wang et al., 2009). The latter value is in line with that estimated for the hippocampal basket cell-granule cell inhibitory synapses (Bucurenciu et al., 2008). These converging results from different synapses not only reconcile opposing views with respect to how VGCCs are coupled to vesicular fusion, but also suggest that microdomain and nanodomain coupling modalities at any given synapse are highly dependent on its functionality and developmental stages.

Although Sept5 filaments do not appear to directly participate in fusion, our evidence implicates a critical role of septin filaments, more specifically Sept5, in the priming/docking of SVs at the prefusion stage. Recent studies suggest that fusion competent SVs in the RRP after “molecular priming” may undergo “positional priming” before the final fusion step can take place (Wadel et al., 2007; Neher and Sakaba, 2008). We suggest that positional priming contains at least two physical components: (1) vertical distance between SVs and AZs, and (2) lateral distance between SVs and VGCCs. Although it is not known how many SNARE complexes are precisely required for membrane fusion between SVs and AZs, an atomic force microscopic study indicates that increasing number of zippered SNARE pairs shortens the vertical distance between two membranes, for example, from 18 nm with one SNARE pair down to 5 nm with four SNARE pairs (Yersin et al., 2003). Septin filaments are composed of multiples of 25 nm unitary length with both ends capable of binding to 7 s SNARE complexes via syntaxin on either SVs and/or AZs. This binding may be of low affinity and simply reduces the likelihood of forming fully zippered state of SNAREs and/or the number of engaged SNAREs, increasing the docking distance of SVs relative to AZs and the energy barrier for fusion. This makes them an ideal spatial substrate for positional priming of SVs to preferred release sites near AZs. This view is supported by our morphological and functional analyses in immature $Sept5^{+/+}$ and $Sept5^{-/-}$ synapses (Figures 2, 3, and 7), in which we showed that there are significantly more tightly docked SVs in release sites devoid of Sept5, and that deletion of Sept5 or functional inhibition of Sept5 with Borg3 peptides or SP20 antibodies imparts striking signature features (Figures 3, 4, and 6) of a “nanodomain” coupling modality. These include both resistance to the slow buffer EGTA and low Ca^{2+} channel/domain cooperativity m.

Acute disruption of Sept5 filaments with antibody injections into immature $Sept5^{+/+}$ calyces significantly lowered Ca^{2+} channel/domain cooperativity with m value from 5.5 to 3.5

(Figure 6), supporting the idea that removal of physical filamentous barriers allows SV docking closer to AZs where VGCCs presumably reside (Figure 7). It however should be noted that the latter value (i.e., 3.5) is substantially higher than that for mature *Sept5*$^{+/+}$ synapses (m = 2.7), and so is the m value for immature *Sept5*$^{-/-}$ synapses (m = 3.3). This suggests that further tightening of the lateral distance between VGCCs and SVs has to take place to account for continued decline in m during further maturation and possibly to a typical distance of ~20 nm for the nanodomain modality as mentioned above. Sept5 filaments are not known to interact with VGCCs, but our data do not exclude their involvement in regulating lateral distance between these channels and docked SVs. Such a short distance would allow close physical interactions between VGCCs and synaptic proteins, as proposed for syntaxin, Rim, synaptotagmin, CASK, etc. (Catterall, 1999; Evans and Zamponi, 2006; Kiyonaka et al., 2007) to effectively mediate transmitter release upon Ca^{2+} entry through VGCCs during an AP.

Our results presented here do not however rule out the engagement of other septin isoforms and synaptic proteins in different steps of positional priming (Neher and Sakaba, 2008; Young and Neher, 2009). In fact, it is likely that Sept5 forms hetero-oligomers with other septin isoforms (Kinoshita, 2003). This is based on the observation that injections of Borg3 peptide, which may target other septins, remained marginally effective in enhancing transmitter release at *Sept5*$^{-/-}$ synapses. In contrast, SP20 antibody produced a robust potentiation in *Sept5*$^{+/+}$ synapses but was completely ineffective in immature *Sept5*$^{-/-}$ synapses. This evidence, along with its strong subsynaptic targeting to AZs and functional phenotypes, leads us to conclude that Sept5 is likely a core molecular substrate that serves as a permissive gate for positional priming of SVs, regardless of their homo- or hetero-oligomers composition. Although a lack of reliable assays has precluded precise topographic mapping of VGCCs and their developmental remodeling at release sites, our evidence, particularly those showing acute transformation from microdomain to nanodomain coupling, firmly establishes that these release modalities are distinct physical entities readily distinguished by the developmental reorganization of Sept5 at the calyx of Held and perhaps other synapses.

EXPERIMENTAL PROCEDURES

Slice Preparation

Mice were housed in the facility certified by the Canadian Council of Animal Care and used for this study according to a protocol approved by the Hospital for Sick Children Animal Care Committee. Brainstem slices were prepared from P8–P19 mice of wild-type and Sept5 knockout genotype (CD1 strain). After decapitation with a small guillotine, brains were immediately immersed into semi-frozen artificial cerebral spinal fluid (ACSF) containing the following (in mM): 125 NaCl, 2.5 KCl, 10 glucose, 1.25 NaH_2PO_4, 2 Na-pyruvate, 3 *myo*-inositol, 0.5 ascorbic acid, 26 $NaHCO_3$, 1 $MgCl_2$, and 2 $CaCl_2$ at a pH of 7.3 when oxygenated (95% O_2 and 5% CO_2). Transverse slices of the auditory brainstem containing the medial nucleus of the trapezoid body (MNTB) were cut at a thickness of 200–250 μm using a microtome (VT1000S; Leica, Nussloch, Germany) followed by incubation at 37°C

for 1 hr before experimentation. All electrophysiological experiments were performed at room temperature (~22°C).

Electrophysiology

All recordings were made with a dual-channel amplifier (MultiClamp 700A; Molecular Devices, Union City, CA) in aCSF supplemented with bicuculline (10 μM) and strychnine (1 μM) to block inhibitory inputs. Patch electrodes typically had resistances of 4–6 and 2.5–3 MΩ for presynaptic and postsynaptic recordings, respectively. For voltage-clamp recordings, presynaptic and postsynaptic series resistances were 6–15 MΩ (<10 MΩ in the majority of recordings) and 3–7 MΩ, respectively, and compensated to 90%. The holding potential was −80 and −60 mV for presynaptic terminals and postsynaptic neurons, respectively. Intracellular solution for all postsynaptic recordings contained the following (in mM): 97.5 K-gluconate, 32.5 CsCl, 5 EGTA, 10 HEPES, 1 $MgCl_2$, 30 TEA, and 3 lidocaine *N*-ethyl bromide (pH 7.2). Whenever presynaptic Ca^{2+} currents were recorded, intracellular recording solution contained the following (in mM): 110 $CsCl_2$, 40 HEPES, 0.5 EGTA, 1 $MgCl_2$, 2 ATP, 0.5 GTP, 12 phosphocreatine, 20 TEA, 3 K-glutamate (pH adjusted to 7.3 with CsOH). For isolation of presynaptic Ca^{2+} currents, tetrodotoxin (0.5 μM), tetraethylammonium (TEA; 10 mM), and 4-aminopyridine (0.3 mM) were added to block Na^+ and K^+ channels, while $[Ca^{2+}]_e$ was reduced to 1 mM to improve the quality of voltage clamp. Presynaptic Ca^{2+} currents were evoked by the voltage command protocols indicated in the text, and leak subtraction was done with the on-line P/4 protocol. For experiments in which real action potentials (AP_I) were applied as presynaptic voltage-command (see Figure 3), we used a prerecorded AP from an immature P10 calyx, which was fed back into amplifier as stimulation files (Axon Text File) through pClamp 9 software at the same sampling frequency as their acquisition (50 kHz). For action potential like paradigm (−80 to +60 mV steps; 0.1 ms incremental increases in plateau time), on- and off-time of command voltage were set at 0.2 ms. For paired presynaptic current-clamp and postsynaptic voltage-clamp recordings, afferent axons were stimulated at 30%–50% above threshold delivered through a Master8 stimulator (A.M.P. Instruments, Jerusalem, Israel). Presynaptic pipettes were filled with a solution containing the following (in mM): 97.5 K-gluconate, 32.5 KCl, 0.5 EGTA, 40 HEPES, 1 $MgCl_2$, and 3 K-glutamate (pH 7.3), supplemented with SP20 antibody (1:2000, Mouse-anti-Septin 5, 200 μg/ml; Santa Cruz Biotech) or Borg BD3 peptide (0.5 ng/ml), except for EGTA injection experiments in which 0.5 mM EGTA was replaced by 10 mM EGTA. Reagents were from Sigma (St. Louis, MO), Tocris Cookson (Bristol, UK), and Alomone Labs (Jerusalem, Israel).

Data Acquisition and Analyses

Data were acquired on-line, filtered at 4 kHz, digitized at 50 kHz, and analyzed off-line using the pClamp 9 software package, MiniAnalysis (Synaptosoft, Decatur, GA) and Excel 2000 (Microsoft, Redmond, WA). For cooperativity analysis, area integrals for both Ca^{2+} currents and EPSCs were detected using analysis windows that began at the onset of Ca^{2+} currents and EPSCs and ended at the points that contain entire area of Ca^{2+} tail current and EPSC that decays to the 10% of its peak amplitude. Current integrals were normalized to the maximal value (100%). The logarithms of normalized area values within their linear range were plotted against each other and the Least-squares linear regression was performed using

Excel 2000 to obtain the slope value defined as *m*, the cooperativity. Synaptic delay was defines as the time difference between the peak of I_{Ca} and the onset of I_{EPSC} by the "maximal curvature" method (Fedchyshyn and Wang, 2007). For the measurement of replenishment of RRP, the area integral of each EPSCs was subtracted by the average area integral of the last five EPSCs in the second train of stimuli to deduct the contribution of the steady state. Subsequently, the total integral of the second train of EPSCs was divided by that of the first train to estimate the percentage of recovery at various intervals. Statistical tests of significance were two-tailed, unpaired Student's t tests assuming unequal variances with a p value cutoff of <0.05 or in some cases K-S two-sample tests were used to determine significance, when data distributions deviated from normality, with a p value cutoff of <0.05. Data were expressed as the mean ± standard error from a population of synapses (*n*).

Production of Borg Peptide

The BD3 domain was amplified out of a cDNA encoding BORG3 (kindly provided by Ian Macara, U. Virginia) by PCR and the PCR product was cloned into pQE30. The construct was confirmed by sequencing and transformed into *E. coli* BL21 cells. Expression of the recombinant peptide was induced with 0.5 mM IPTG for 4 hr during growth in LB broth at 37°C. Recombinant peptide isolation involved pelleting and lysis of the cells twice with a French Press in PBS containing protease inhibitors. The lysate was cleared and added to Ni-NTA agarose for 1 hr before washing several times in PBS containing 300 mM NaCl and 20 mM imidazole. The washed peptide was eluted from the beads using 500 mM imidazole in PBS with 300 mM NaCl. The imidazole was removed using a desalting column. The final Borg peptide was dialyzed into K^+-based intracellular recording solution for electrophysiological experiments.

Immunohistochemistry and Image Acquisition

Brainstem slices were acquired at a thickness of 200 μm as described for electrophysiology and then fixed in 4% paraformaldehyde in PBS for 30 min. Following several rinses in PBS, permeabilization in 0.2% Triton X-100 and blocking with a M.O.M. kit (Vector Laboratories), slices were incubated overnight at 4°C in primary antibody (1:50, Mouse-anti-Septin 5, SP20 200 μg/ml, Santa Cruz Biotech; 1:400 Mouse anti-Bassoon, SAP7F407 1mg/ml, Assay Designs). After several rinses in PBS, slices were incubated for 2 hr in secondary antibody conjugated to Cy3 (1:500, Goat-anti-Mouse, 1.5 mg/ml, Jackson ImmunoResearch). For colabeling experiments, same procedures after the first round of staining were repeated with primary antibody to vesicular glutamate transporter-1 (vGLUT1) (1:1000, guinea pig anti-vGLUT1; Millipore) and secondary antibody conjugated to Alexa 488 (1:500, goat anti-guinea pig, 2 mg/ml, Molecular Probes). Slices were mounted and coverslipped using Vectashield (Vector Laboratories).

Confocal images and z stacks were acquired with a Zeiss LSM 510 Multiphoton Laser Scanning Microscope equipped with 488 and 514 nm argon laser lines to visualize the fluorochromes Alexa 488 and Cy3, respectively. Confocal scans for each fluorochrome were acquired sequentially using a 63× (N.A. 1.4) oil objective and the appropriate dichroic filters (MBS 488 and MBS 514). Emission spectra were adjusted such that the wavelength of emitted fluorescence following Alexa 488 and Cy3 excitation did not overlap. To maximize

the image quality, the intensity signal from each channel was adjusted to just below saturation levels. Line intensity scans for each channel were normalized to the peak intensity measured along the line scan. 3D reconstructions were generated using Volocity 4.1 (Improvision). Brightness and contrast were adjusted with Volocity 4.1.

Electron Microscopy (EM) and Quantitative Analyses

For conventional EM experiments (Figures 2E and 2F), brainstem slices were prepared as described above but cut at a thickness of 300 μm. Following incubation (1 hr), slices were placed in fixative (2.5% gluteraldehyde in 0.1Mcacodylate buffer, pH 7.4) for 2 hr and then washed in 0.1 M cacodylate buffer four times at 10 min intervals. Sections were postfixed in osmium tetroxide (1% in 0.1Mcacodylate buffer), saturated in uranyl acetate (1% in water) for 1 hr, and washed four times for 10 min in dH_2O. Sections were then dehydrated and flatly embedded in Durcapan resin (Fluka, EMS, Hatfield PA). Serial ultrathin sections were cut at the University of Toronto electron microscopy facility using an RMC MT7000 ultramicrotome to a thickness of 80 nm and collected onto high-transmission copper grids (50-mesh) and subsequently contrasted with 5% aqueous uranyl acetate. Micrographs were collected with an AT digital camera (6 MP) inside a Hitachi 7000 transmission electron microscope at a filament voltage of 75 kV. SV-AZ separation was evaluated by measuring the distance between the closest points on the vesicle membrane and the visually identifiable AZ membrane. SVs within two vesicle diameters (~100 nm) of the AZ were measured with those separated by less than 10 nm being considered physically “docked.” Normalized SV separation distributions were evaluated using OpenLab software (OpenLab, Coventry, UK) and plotted in Microsoft Excel 2000. Approximately 1600 SV separation measurements were taken from age-matched calyces for the immature (P9) and mature (P17) experimental groups from a minimum of 5 calyces per group. SV separation distances were grouped into 5 nm bins and plotted as noted throughout the text.

For immunogold EM experiments (Figure 7A), mice were first anaesthetized with 20% urethane and then perfused with oxygenated ACSF and fixed with 4% paraformaldehyde through a small needle inserted into the left ventricle of the heart. Brainstems were isolated and sectioned into 0.4–0.5 mm slices. Small tissue pieces containing the MNTB were dissected out from P10 and P17 *Sept5*$^{+/+}$ or *Sept5*$^{-/-}$ mice and postfixed in 4% paraformaldehyde containing 0.1% glutaraldehyde in 0.1 M phosphate buffer (pH = 7.4) overnight, rinsed thoroughly in phosphate buffer and stored at 4°C in PBS containing 20 mM sodium azide. Prior to further processing the tissue was infused with 2.3 M sucrose for several hours and frozen on aluminum cryo ultramicrotomy pins in liquid nitrogen. Ultrathin cryosections were then prepared using a cryo diamond knife and a Leica Ultracut R with an FC4 cryo attachment at −120°C (Leica Microsystems, Willowdale, ON, Canada). Sections were transferred to a formvar-coated nickel grid in a loop of molten sucrose. Grids were then washed twice in 80mM ammonium chloride, followed by several rinses in PBS containing 0.5% BSA and 0.15% glycine. Slices were rinsed in PBS containing 0.5% BSA and then incubated in a monoclonal antibody against Sept5 (1:75) for 1 hr (SP20, mouse-anti-Septin 5, 200 μg/ml, 1:75, Santa Cruz Biotech). Following a thorough rinse in PBS/BSA, the grids were incubated in goat-anti-murine IgG 10 nm gold complexes (SPI supplies, West Chester, PA) for an additional hour. Specimens were rinsed thoroughly in PBS/BSA followed by PBS

and then distilled water. Sections were stabilized in a thin film of methyl cellulose containing 0.2% uranyl acetate and allowed to dry overnight.

Specimens were examined and photographed using a JEOL JEM 1400 transmission electron microscope (tEM) (JEOL USA, Peabody, MA) and images were obtained using a CCD camera (AMT, Danvers, MA). Presynaptic calyces were readily identified at low magnifications with numerous synaptic vesicles and mitochondria within long continuum of double-layer sheets engulfing postsynaptic neurons. Gold particle density determinations and synaptic distribution characterizations were done using Image J (NIH, Bethesda, MD). Synaptic gold particle density was determined for 50 synapses from both P10 and P17 mice and expressed as the number of particles observed per micron of membrane. To quantify the distribution of gold particles near the AZs of P10 and P17 synapses, 100 active zones from each age group (3 mice/each) was examined. We first determined how many synapses contained gold particles positioned directly at the center of the active zone. This was repeated to examine how many synapses contained particles located within 0.5 μm from the center of the AZ using 0.1 μm increments. This analysis reflects the probability of observing Septin 5 along the AZ and peri-AZ regions of immature and mature synapses. Data are expressed as mean ± standard error, and significance was determined using student's t test and a multivariate ANOVA analysis.

Antibody Injection into Chinese Hamster Ovary (CHO) Cells and Image Acquisition

CHO cells were maintained in F12 medium containing 10% fetal calf serum. For transfection experiments, CHO cells were split into 12 well dishes onto coverslips at low density and transfected with GFP-Sept5 or GFP-actin using Fugene HD (Roche) in serum free medium. One microgram of each DNA was mixed with three microliters of Fugene HD and added to serum free medium for 15 hr. Medium was then replaced with cell culture medium and prepared for imaging. CHO cells expressing GFP-labeled Sept5 or actin filaments were imaged using a Zeiss LSM 710 confocal microscope equipped with a 63× (1.0 N.A) water immersion objective. A 488 nm argon laser line was used to excite GFP. To visualize the effects of SP20 on septin5 filaments in CHO cells, high resolution images were captured as a time series. Image scanning began ~30 s prior to the injection of SP20 into CHO cells and continued for the next 5 min. Time series imaging following SP20 injection into CHO cells expressing GFP-labeled actin filaments was repeated under the same conditions. Images were processed using Volocity 4.1 (Improvision). For injection of SP20 into CHO cells, the extracellular solution contained (in mM): 145 NaCl, 5 KCl, 2 $CaCl_2$, 1 $MgCl_2$, 10 Glucose, 10 HEPES (pH adjusted to 7.3) with NaOH. Patch electrodes had resistances of 4–6 MΩ and were filled with the intracellular solution including (in mM): 97.5 K-gluconate, 32.5 KCl, 0.5 EGTA, 40 HEPES, 1 $MgCl_2$ (pH 7.3), supplemented with SP20 antibody (from 1:200 to 1:2000 dilutions). The CHO cells were held at −60 mV after breakthrough of the membrane and monitored with a dual-channel amplifier (MultiClamp 700B; Molecular Devices, Union City, CA).

Acknowledgments

This work was supported by individual operating grants (MOP-143867 and MOP-97950) from Canadian Institutes of Health Research (CIHR) (to L.-Y.W. and W.S.T., respectively). W.S.T. and L.-Y.W. are the recipients of Canada

Research Chairs. We thank Drs. Milton Charlton and Harold Atwood for critically reviewing an early version of this paper and other members of the Wang and Trimble labs for technical assistance, comments and discussions.

References

Adler EM, Augustine GJ, Duffy SN, Charlton MP. Alien intracellular calcium chelators attenuate neurotransmitter release at the squid giant synapse. J Neurosci. 1991; 11:1496–1507. [PubMed: 1675264]

Augustine GJ. Regulation of transmitter release at the squid giant synapse by presynaptic delayed rectifier potassium current. J Physiol. 1990; 431:343–364. [PubMed: 1983120]

Augustine GJ, Charlton MP, Smith SJ. Calcium action in synaptic transmitter release. Annu Rev Neurosci. 1987; 10:633–693. [PubMed: 2436546]

Barral Y, Kinoshita M. Structural insights shed light onto septin assemblies and function. Curr Opin Cell Biol. 2008; 20:12–18. [PubMed: 18242072]

Beites CL, Xie H, Bowser R, Trimble WS. The septin CDCrel-1 binds syntaxin and inhibits exocytosis. Nat Neurosci. 1999; 2:434–439. [PubMed: 10321247]

Beites CL, Campbell KA, Trimble WS. The septin Sept5/CDCrel-1 competes with alpha-SNAP for binding to the SNARE complex. Biochem J. 2005; 385:347–353. [PubMed: 15355307]

Borst JGG, Sakmann B. Facilitation of presynaptic calcium currents in the rat brainstem. J Physiol. 1998; 513:149–155. [PubMed: 9782166]

Borst JGG, Sakmann B. Effect of changes in action potential shape on calcium currents and transmitter release in a calyx-type synapse of the rat auditory brainstem. Philos Trans R Soc Lond B Biol Sci. 1999; 354:347–355. [PubMed: 10212483]

Borst JGG, Helmchen F, Sakmann B. Pre- and postsynaptic whole-cell recordings in the medial nucleus of the trapezoid body of the rat. J Physiol. 1995; 489:825–840. [PubMed: 8788946]

Bucurenciu I, Kulik A, Schwaller B, Frotscher M, Jonas P. Nanodomain coupling between Ca2+ channels and Ca^{2+} sensors promotes fast and efficient transmitter release at a cortical GABAergic synapse. Neuron. 2008; 57:536–545. [PubMed: 18304483]

Catterall WA. Interactions of presynaptic Ca2+ channels and snare proteins in neurotransmitter release. Ann N Y Acad Sci. 1999; 868:144–159. [PubMed: 10414292]

Dresbach T, Qualmann B, Kessels MM, Garner CC, Gundelfinger ED. The presynaptic cytomatrix of brain synapses. Cell Mol Life Sci. 2001; 58:94–116. [PubMed: 11229820]

Evans RM, Zamponi GW. Presynaptic Ca^{2+} channels—integration centers for neuronal signaling pathways. Trends Neurosci. 2006; 29:617–624. [PubMed: 16942804]

Fedchyshyn MJ, Wang LY. Developmental transformation of the release modality at the calyx of Held synapse. J Neurosci. 2005; 25:4131–4140. [PubMed: 15843616]

Fedchyshyn MJ, Wang LY. Activity-dependent changes in temporal components of neurotransmission at the juvenile mouse calyx of Held synapse. J Physiol. 2007; 581:581–602. [PubMed: 17347264]

Geiger JRP, Jonas P. Dynamic control of presynaptic Ca(2+) inflow by fast-inactivating K(+) channels in hippocampal mossy fiber boutons. Neuron. 2000; 28:927–939. [PubMed: 11163277]

Gentile L, Stanley EF. A unified model of presynaptic release site gating by calcium channel domains. Eur J Neurosci. 2005; 21:278–282. [PubMed: 15654866]

Hirokawa N, Sobue K, Kanda K, Harada A, Yorifuji H. The cytoskeletal architecture of the presynaptic terminal and molecular structure of synapsin 1. J Cell Biol. 1989; 108:111–126. [PubMed: 2536030]

Hsu SC, Hazuka CD, Roth R, Foletti DL, Heuser J, Scheller RH. Subunit composition, protein interactions, and structures of the mammalian brain sec6/8 complex and septin filaments. Neuron. 1998; 20:1111–1122. [PubMed: 9655500]

Ihara M, Tomimoto H, Kitayama H, Morioka Y, Akiguchi I, Shibasaki H, Noda M, Kinoshita M. Association of the cytoskeletal GTP-binding protein Sept4/H5 with cytoplasmic inclusions found in Parkinson's disease and other synucleinopathies. J Biol Chem. 2003; 278:24095–24102. [PubMed: 12695511]

Iwasaki S, Takahashi T. Developmental regulation of transmitter release at the calyx of Held in rat auditory brainstem. J Physiol. 2001; 534:861–871. [PubMed: 11483715]

Joberty G, Perlungher RR, Sheffield PJ, Kinoshita M, Noda M, Haystead T, Macara IG. Borg proteins control septin organization and are negatively regulated by Cdc42. Nat Cell Biol. 2001; 3:861–866. [PubMed: 11584266]

Joshi I, Wang LY. Developmental profiles of glutamate receptors and synaptic transmission at a single synapse in the mouse auditory brainstem. J Physiol. 2002; 540:861–873. [PubMed: 11986375]

Kinoshita M. Assembly of mammalian septins. J Biochem. 2003; 134:491–496. [PubMed: 14607974]

Kiyonaka S, Wakamori M, Miki T, Uriu Y, Nonaka M, Bito H, Beedle AM, Mori E, Hara Y, De Waard M, et al. RIM1 confers sustained activity and neurotransmitter vesicle anchoring to presynaptic Ca2+ channels. Nat Neurosci. 2007; 10:691–701. [PubMed: 17496890]

Kochubey O, Han YY, Schneggenburger R. Developmental regulation of the intracellular Ca2+ sensitivity of vesicle fusion and Ca2+-secretion coupling at the rat calyx of Held. J Physiol. 2009; 587:3009–3023. [PubMed: 19403608]

Leão RM, von Gersdorff H. Synaptic vesicle pool size, release probability and synaptic depression are sensitive to Ca2+ buffering capacity in the developing rat calyx of Held. Braz J Med Biol Res. 2009; 42:94–104. [PubMed: 19219302]

Matveev V, Bertram R, Sherman A. Ca2+ current versus Ca2+ channel cooperativity of exocytosis. J Neurosci. 2009; 29:12196–12209. [PubMed: 19793978]

Meinrenken CJ, Borst JGG, Sakmann B. Calcium secretion coupling at calyx of held governed by nonuniform channel-vesicle topography. J Neurosci. 2002; 22:1648–1667. [PubMed: 11880495]

Meinrenken CJ, Borst JGG, Sakmann B. Local routes revisited: the space and time dependence of the Ca2+ signal for phasic transmitter release at the rat calyx of Held. J Physiol. 2003; 547:665–689. [PubMed: 12562955]

Mintz IM, Sabatini BL, Regehr WG. Calcium control of transmitter release at a cerebellar synapse. Neuron. 1995; 15:675–688. [PubMed: 7546746]

Naraghi M, Neher E. Linearized buffered Ca2+ diffusion in microdomains and its implications for calculation of [Ca2+] at the mouth of a calcium channel. J Neurosci. 1997; 17:6961–6973. [PubMed: 9278532]

Neher E, Sakaba T. Multiple roles of calcium ions in the regulation of neurotransmitter release. Neuron. 2008; 59:861–872. [PubMed: 18817727]

Roberts WM, Jacobs RA, Hudspeth AJ. Colocalization of ion channels involved in frequency selectivity and synaptic transmission at presynaptic active zones of hair cells. J Neurosci. 1990; 10:3664–3684. [PubMed: 1700083]

Rollenhagen A, Lübke JHR. The morphology of excitatory central synapses: from structure to function. Cell Tissue Res. 2006; 326:221–237. [PubMed: 16932936]

Sabatini BL, Regehr WG. Control of neurotransmitter release by presynaptic waveform at the granule cell to Purkinje cell synapse. J Neurosci. 1997; 17:3425–3435. [PubMed: 9133368]

Schneggenburger R, Forsythe ID. The calyx of Held. Cell Tissue Res. 2006; 326:311–337. [PubMed: 16896951]

Schneggenburger R, Meyer AC, Neher E. Released fraction and total size of a pool of immediately available transmitter quanta at a calyx synapse. Neuron. 1999; 23:399–409. [PubMed: 10399944]

Schneggenburger R, Sakaba T, Neher E. Vesicle pools and short-term synaptic depression: lessons from a large synapse. Trends Neurosci. 2002; 25:206–212. [PubMed: 11998689]

Schoch S, Gundelfinger ED. Molecular organization of the presynaptic active zone. Cell Tissue Res. 2006; 326:379–391. [PubMed: 16865347]

Sheffield PJ, Oliver CJ, Kremer BE, Sheng ST, Shao ZF, Macara IG. Borg/septin interactions and the assembly of mammalian septin heterodimers, trimers, and filaments. J Biol Chem. 2003; 278:3483–3488. [PubMed: 12446710]

Siksou L, Rostaing P, Lechaire JP, Boudier T, Ohtsuka T, Fejtová A, Kao HT, Greengard P, Gundelfinger ED, Triller A, Marty S. Three-dimensional architecture of presynaptic terminal cytomatrix. J Neurosci. 2007; 27:6868–6877. [PubMed: 17596435]

Stanley EF. Single calcium channels on a cholinergic presynaptic nerve terminal. Neuron. 1991; 7:585–591. [PubMed: 1657055]

Surka MC, Tsang CW, Trimble WS. The mammalian septin MSF localizes with microtubules and is required for completion of cytokinesis. Mol Biol Cell. 2002; 13:3532–3545. [PubMed: 12388755]

Suzuki G, Harper KM, Hiramoto T, Sawamura T, Lee M, Kang G, Tanigaki K, Buell M, Geyer MA, Trimble WS, et al. Sept5 deficiency exerts pleiotropic influence on affective behaviors and cognitive functions in mice. Hum Mol Genet. 2009; 18:1652–1660. [PubMed: 19240081]

Tada T, Simonetta A, Batterton M, Kinoshita M, Edbauer D, Sheng M. Role of Septin cytoskeleton in spine morphogenesis and dendrite development in neurons. Curr Biol. 2007; 17:1752–1758. [PubMed: 17935993]

Taschenberger H, von Gersdorff H. Fine-tuning an auditory synapse for speed and fidelity: developmental changes in presynaptic waveform, EPSC kinetics, and synaptic plasticity. J Neurosci. 2000; 20:9162–9173. [PubMed: 11124994]

Taschenberger H, Leão RM, Rowland KC, Spirou GA, von Gersdorff H. Optimizing synaptic architecture and efficiency for high-frequency transmission. Neuron. 2002; 36:1127–1143. [PubMed: 12495627]

Trussell LO. Cellular mechanisms for preservation of timing in central auditory pathways. Curr Opin Neurobiol. 1997; 7:487–492. [PubMed: 9287194]

Tsang CW, Fedchyshyn M, Harrison J, Xie H, Xue J, Robinson PJ, Wang LY, Trimble WS. Superfluous role of mammalian septins 3 and 5 in neuronal development and synaptic transmission. Mol Cell Biol. 2008; 28:7012–7029. [PubMed: 18809578]

von Gersdorff H, Borst JGG. Short-term plasticity at the calyx of held. Nat Rev Neurosci. 2002; 3:53–64. [PubMed: 11823805]

Wadel K, Neher E, Sakaba T. The coupling between synaptic vesicles and Ca2+ channels determines fast neurotransmitter release. Neuron. 2007; 53:563–575. [PubMed: 17296557]

Walikonis RS, Jensen ON, Mann M, Provance DW Jr, Mercer JA, Kennedy MB. Identification of proteins in the postsynaptic density fraction by mass spectrometry. J Neurosci. 2000; 20:4069–4080. [PubMed: 10818142]

Wang LY, Kaczmarek LK. High-frequency firing helps replenish the readily releasable pool of synaptic vesicles. Nature. 1998; 394:384–388. [PubMed: 9690475]

Wang LY, Neher E, Taschenberger H. Synaptic vesicles in mature calyx of Held synapses sense higher nanodomain calcium concentrations during action potential-evoked glutamate release. J Neurosci. 2008; 28:14450–14458. [PubMed: 19118179]

Wang LY, Fedchyshyn M, Yang YM. Action potential evoked transmitter release in central synapses: insights from the developing calyx of Held. Molecular Brain. 2009; 2:36. [PubMed: 19939269]

Weirich CS, Erzberger JP, Barral Y. The septin family of GTPases: architecture and dynamics. Nat Rev Mol Cell Biol. 2008; 9:478–489. [PubMed: 18478031]

Wimmer VC, Horstmann H, Groh A, Kuner T. Donut-like topology of synaptic vesicles with a central cluster of mitochondria wrapped into membrane protrusions: a novel structure-function module of the adult calyx of Held. J Neurosci. 2006; 26:109–116. [PubMed: 16399677]

Wu LG, Saggau P. Pharmacological identification of two types of presynaptic voltage-dependent calcium channels at CA3-CA1 synapses of the hippocampus. J Neurosci. 1994; 14:5613–5622. [PubMed: 8083757]

Wu LG, Borst JGG, Sakmann B. R-type Ca2+ currents evoke transmitter release at a rat central synapse. Proc Natl Acad Sci USA. 1998; 95:4720–4725. [PubMed: 9539805]

Xie Y, Vessey JP, Konecna A, Dahm R, Macchi P, Kiebler MA. The GTP-binding protein Septin 7 is critical for dendrite branching and dendritic-spine morphology. Curr Biol. 2007; 17:1746–1751. [PubMed: 17935997]

Yang YM, Wang LY. Amplitude and kinetics of action potential-evoked Ca2+ current and its efficacy in triggering transmitter release at the developing calyx of held synapse. J Neurosci. 2006; 26:5698–5708. [PubMed: 16723526]

Yersin A, Hirling H, Steiner P, Magnin S, Regazzi R, Hüni B, Huguenot P, De los Rios P, Dietler G, Catsicas S, Kasas S. Interactions between synaptic vesicle fusion proteins explored by atomic force microscopy. Proc Natl Acad Sci USA. 2003; 100:8736–8741. [PubMed: 12853568]

Yoshikami D, Bagabaldo Z, Olivera BM. The inhibitory effects of omega-conotoxins on Ca channels and synapses. Ann N Y Acad Sci. 1989; 560:230–248. [PubMed: 2545135]

Young SM Jr, Neher E. Synaptotagmin has an essential function in synaptic vesicle positioning for synchronous release in addition to its role as a calcium sensor. Neuron. 2009; 63:482–496. [PubMed: 19709630]

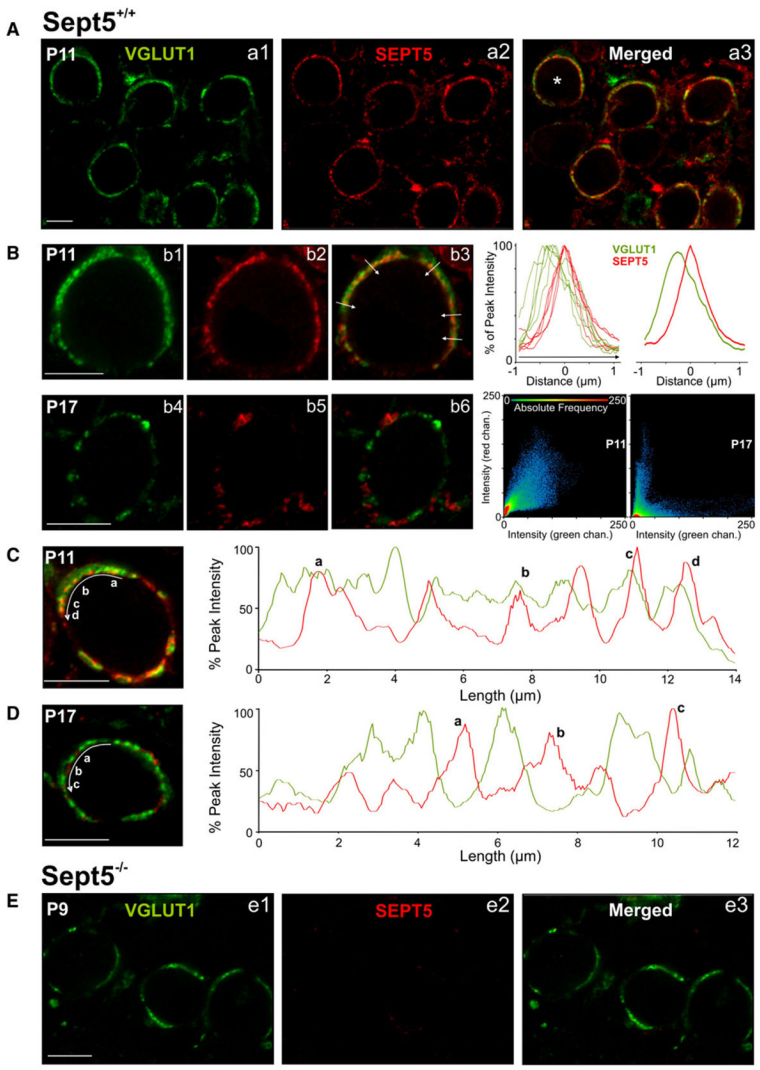

Figure 1. Spatial Localization Patterns of Sept5 in the Developing Calyx of Held Terminals

(A) (a1–a3) Low-power images of vGLUT1 (green) and Sept5 (red) staining in the MNTB from *Sept5*$^{+/+}$ synapses at P11.

(B) (b1–b3) High-power images of vGLUT1 and Sept5 stained cell indicated in a3 (asterisk). White arrows in (b3) indicate the position and direction of line scans performed to measure the fluorescent intensity normalized to the peak intensity of each fluorophore along different regions of the calyx terminal. Result of individual line scans (right) and their average (far right) are displayed and aligned according to the peak intensity of the Sept5 signal. Note the relative positional difference in the peaks of two fluorophores. (b4–b6) High-power image of vGLUT1 and Sept5 stained calyx at P17. To the right, colocalization plots for calyx in (b3) and (b6) showing a strong correlation between Sept5 and vGLUT1 fluorescence in the P11 calyx (r = 0.8) but a weak correlation in the P17 calyx (r = 0.2).

(C) Another co-labeled vGLUT1 and Sept5 calyx terminal at P11. Curved white arrow indicates direction of a line scan performed to measure the fluorescent intensity. The position of the white arrow has been shifted just below measured region for clarity. Letters

correspond to the red peaks indicated in the line scan plots to the right. Note that peaks of septin and vGLUT1 fluorescence sometimes overlap.

(D) Same as (C) but in P17 *Sept5*$^{+/+}$ calyx, showing an approximate reciprocal distribution of vGLUT1 and Sept5.

(E) (e1–e3) vGLUT1 and Sept5 staining in *Sept5*$^{-/-}$ synapses (P9). vGLUT1 visualized with Alexa 488; Sept5 visualized with Cy3.

Scale bars = 9 μm.

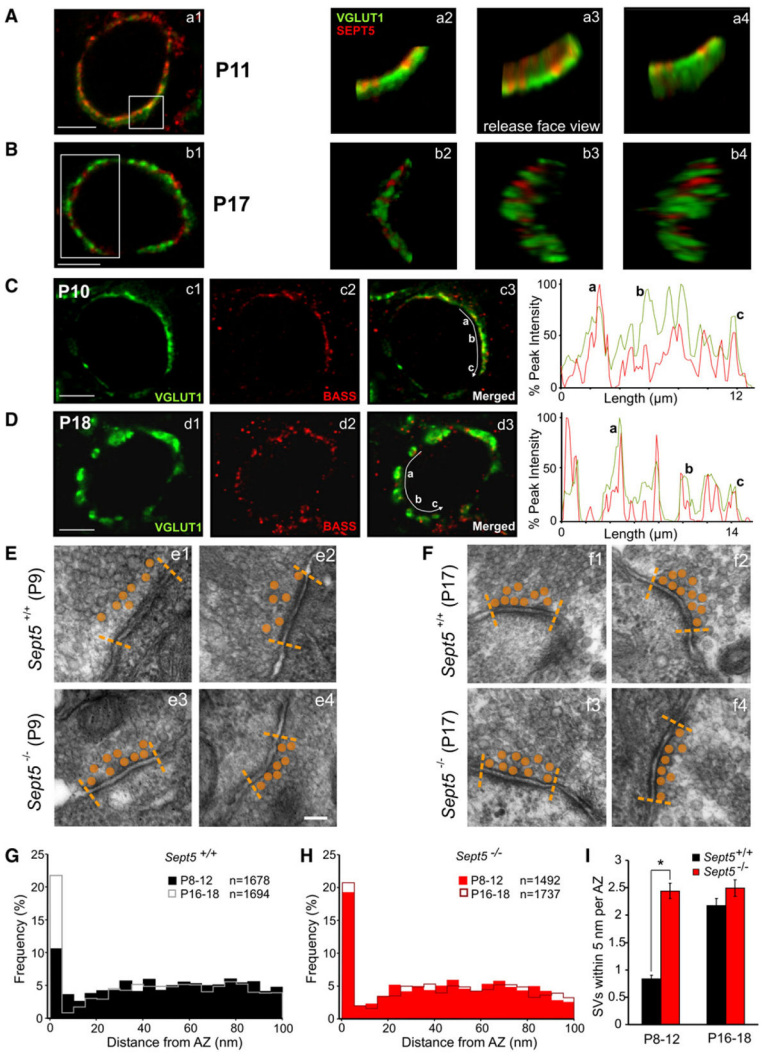

Figure 2. Subsynaptic Organization of SVs and Sept5 in Immature and Mature Calyx of Held Terminals

(A) Images of a P11 *Sept5*$^{+/+}$ calyx costained with vGLUT1 and Sept5 are shown. Boxed region highlights the area of the acquired z stack with enlarged 3D reconstructions displayed to the right. (a2) Reconstruction image with no rotation. (a3) Reconstruction rotated to expose the transmitter release face of the calyx terminal. (a4) Reconstruction rotation to expose opposite side. Note considerable colocalization as shown by yellow color.

(B) Same as (A) but from a P17 *Sept5*$^{+/+}$ calyx showing vGLUT1 and Sept5 occupying segregated regions of the calyx of Held terminal, without colocalization.

(C) Images of a P10 calyx terminal stained with vGLUT1 and Bassoon. Curved white arrow in merged image indicates the position and direction of a line scan (far right) performed to measure the fluorescent intensity normalized to the peak intensity of each fluorophore. The position of the white arrow has been shifted just below measured region for clarity. Letters correspond to the red peaks indicated in the line scan plots to the right.

(D) Same as in (C) but vGLUT1 and Bassoon costaining performed in a P18 calyx terminal. Bassoon labeling was occasionally not colocalized with vGLUT1, which may represent the AZs of minor synaptic inputs known to innervate principle MNTB neurons.

(E and F) EM images, taken from immature *Sept5*$^{+/+}$ (e1 and e2) and *Sept5*$^{-/-}$ (e3 and e4) (P9) and mature *Sept5*$^{+/+}$ (f1 and f2) and *Sept5*$^{-/-}$ (f3 and f4) (P17) synapses, of visually identified AZs. Synaptic vesicles (SV) closest to AZ have been shaded in orange for clarity with AZ boundary denoted by dashed lines. Each image in each panel recorded from a different calyx.

(G and H) Summary of normalized histograms plotting SV distance from AZs for immature and mature *Sept5*$^{+/+}$ (G) and *Sept5*$^{-/-}$ (H) synapses. Immature *Sept5*$^{+/+}$ synapses are indicated in solid black and immature *Sept5*$^{-/-}$ in solid red.

(I) The normalized numbers of SVs within the distance of 5 nm from AZs in immature and mature *Sept5*$^{+/+}$ (black) and *Sept5*$^{-/-}$ (red) synapses.

Scale bars in (A)–(D) = 5 μm and in (E) = 100 nm and also applies to (F). * indicates statistical significance ($p < 0.05$) in this and the following figures.

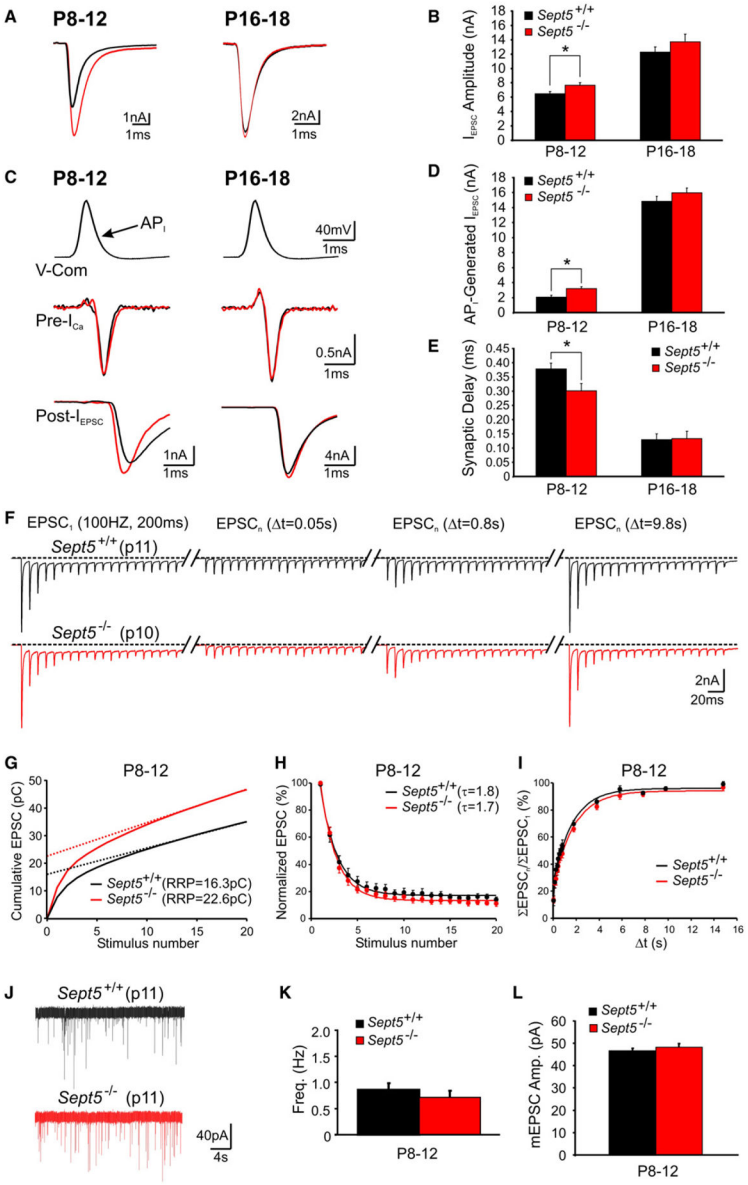

Figure 3. Deletion of Sept5 Enhances Quantal Output and Expands RRP Size

(A) Evoked I_{EPSC} from immature and mature *Sept5*$^{+/+}$ (black) and *Sept5*$^{-/-}$ (red) synapses by afferent stimulation.

(B) Summary data showing average I_{EPSC} amplitude for the experimental conditions shown in (A).

(C) Presynaptic voltage-command AP_I (top panels) with resultant presynaptic I_{Ca} (middle panels) and postsynaptic I_{EPSC} (bottom panels) for immature (left panels) and mature (right panels) *Sept5*$^{+/+}$ and *Sept5*$^{-/-}$ synapses.

(D) Summary data for I_{EPSC} amplitude in response to the AP_I command template.

(E) Summary data of synaptic delay for the conditions shown in (C).

(F) I_{EPSC} in response to two trains of stimuli (100Hz, 200ms) with various intervals from *Sept5*$^{+/+}$ (black) and *Sept5*$^{-/-}$ (red) synapses.

(G) Cumulative current integral as a function of stimulus number for immature *Sept5*$^{+/+}$ and *Sept5*$^{-/-}$ synapses. Dashed lines represent least-squares linear fits to the steady-state EPSCs with highest R^2-value back-extrapolated to time 0 (i.e., the cumulative EPSCs or RRP) (Schneggenburger et al., 1999).

(H) Summary plot of normalized area integrals of EPSCs to the initial EPSCs during a train of stimuli, against the stimulus numbers.

(I) A summary showing the recovery of the total area integral of EPSCs as a function of the intervals between these two trains of stimuli for immature *Sept5*$^{+/+}$ (black) and *Sept5*$^{-/-}$ (red) synapses.

(J) mEPSC recordings (30 s) from immature *Sept5*$^{+/+}$ and *Sept5*$^{-/-}$ synapses.

(K and L) Summary data showing mEPSC frequency (G) and amplitude (H) for *Sept5*$^{+/+}$ and *Sept5*$^{-/-}$ synapses.

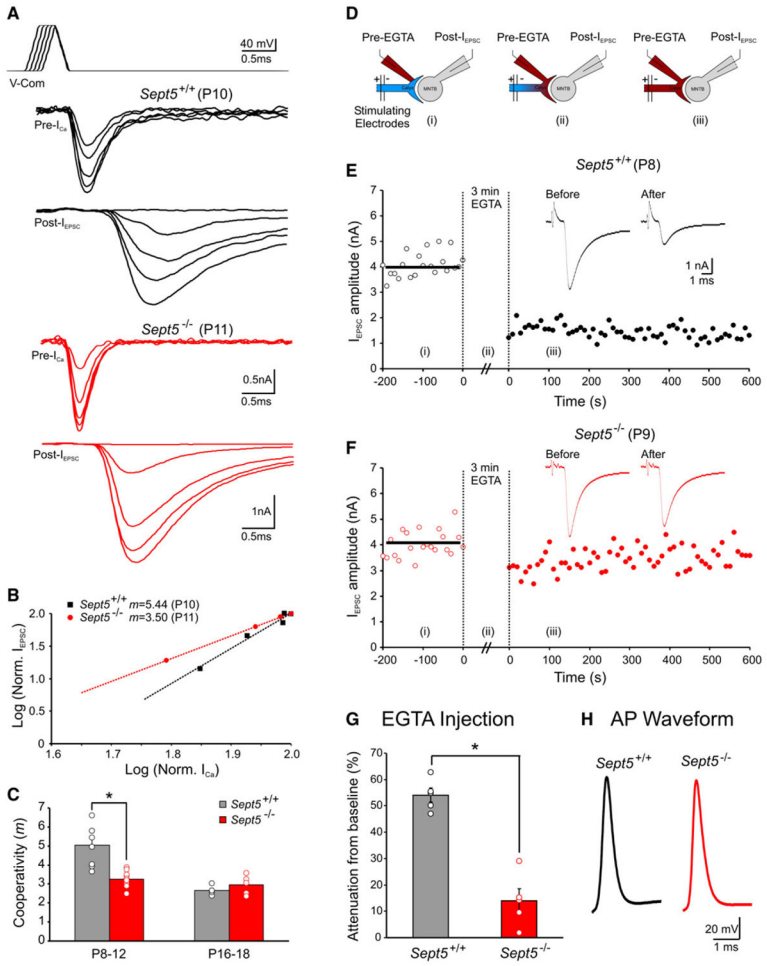

Figure 4. Nanodomain coupling of VGCCs and SVs in immature *Sept5*$^{-/-}$ Synapses

(A) Paired presynaptic I_{Ca} and postsynaptic I_{EPSC} recordings in response to the voltage-command protocol (top panel) from *Sept5*$^{+/+}$ (black) and *Sept5*$^{-/-}$ (red) synapses.

(B) Log-Log plot of normalized I_{Ca} versus I_{EPSC} for the recordings in (A). Dashed lines are least-squares regression fits.

(C) Summary data showing *m* values for immature and mature *Sept5*$^{+/+}$ and *Sept5*$^{-/-}$ synapses. The black and red circles represent individual data points for *Sept5*$^{+/+}$ and *Sept5*$^{-/-}$ synapses, respectively, in this and the following figures.

(D) Schematic illustrating paired recording configurations for Ca^{2+} buffer injections into presynaptic terminals with postsynaptic whole-cell voltage-clamp recordings of I_{EPSC}: *i*, presynaptic cell-attached mode for baseline measurements; *ii*, buffer infusion into the terminal; and *iii*, re-establishing paired recordings of presynaptic APs and EPSCs after buffer equilibrium. Presynaptic resting potential was ~−75 mV.

(E and F) Amplitudes of I_{EPSC} before and after 10mMEGTA injections plotted against time from *Sept5*$^{+/+}$ (E) and *Sept5*$^{-/-}$ (F) synapses. Raw traces (insets) with or without EGTA are shown for comparison.

(G) Plot of the extent of EGTA-induced attenuation for immature *Sept5*$^{+/+}$ and *Sept5*$^{-/-}$ synapses, which was calculated as the ratio between the reduction of the mean amplitude of EPSCs after EGTA injections and the mean amplitude of baseline EPSCs (100%).
(H) Sample AP waveforms from immature *Sept5*$^{+/+}$ and *Sept5*$^{-/-}$ calyces.

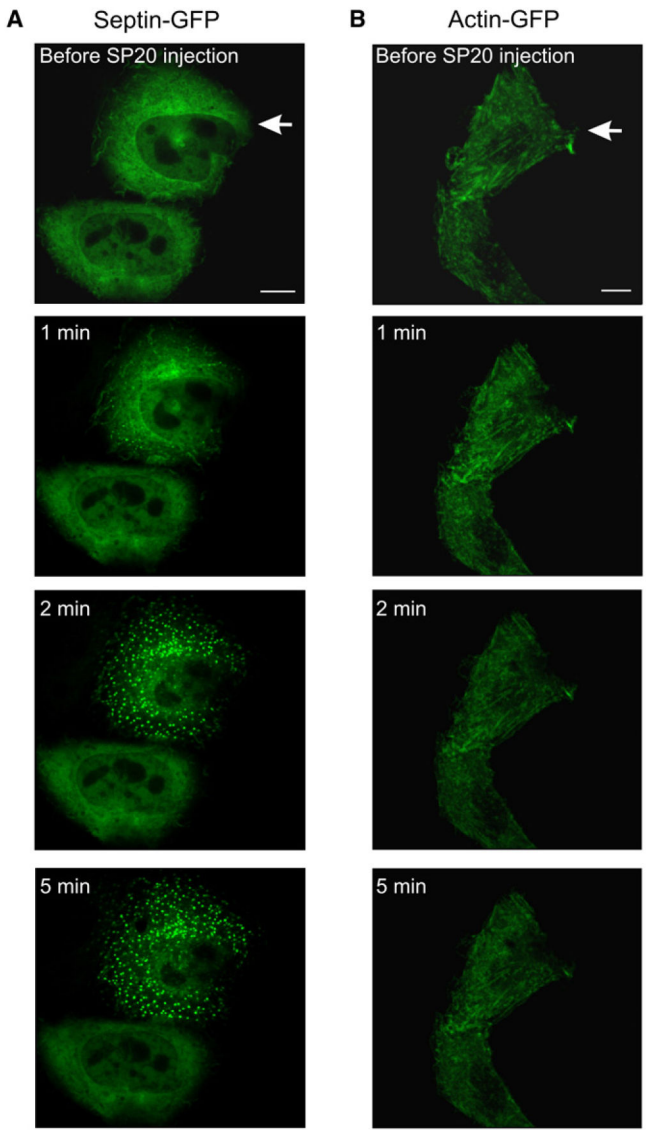

Figure 5. Disassembly of Sept5 Filaments using a Sept5 Monoclonal Antibody (SP20)

Top row: Confocal images displaying overexpressed GFP-tagged Sept5 (A) and actin (B) filaments in Chinese hamster ovary (CHO) cells before SP20 injection (1:200). Subsequent images, shown at 1, 2, and 5 min after SP20 injections captured during time series imaging. Arrow indicates injected cell. Scale bars = 100 μm.

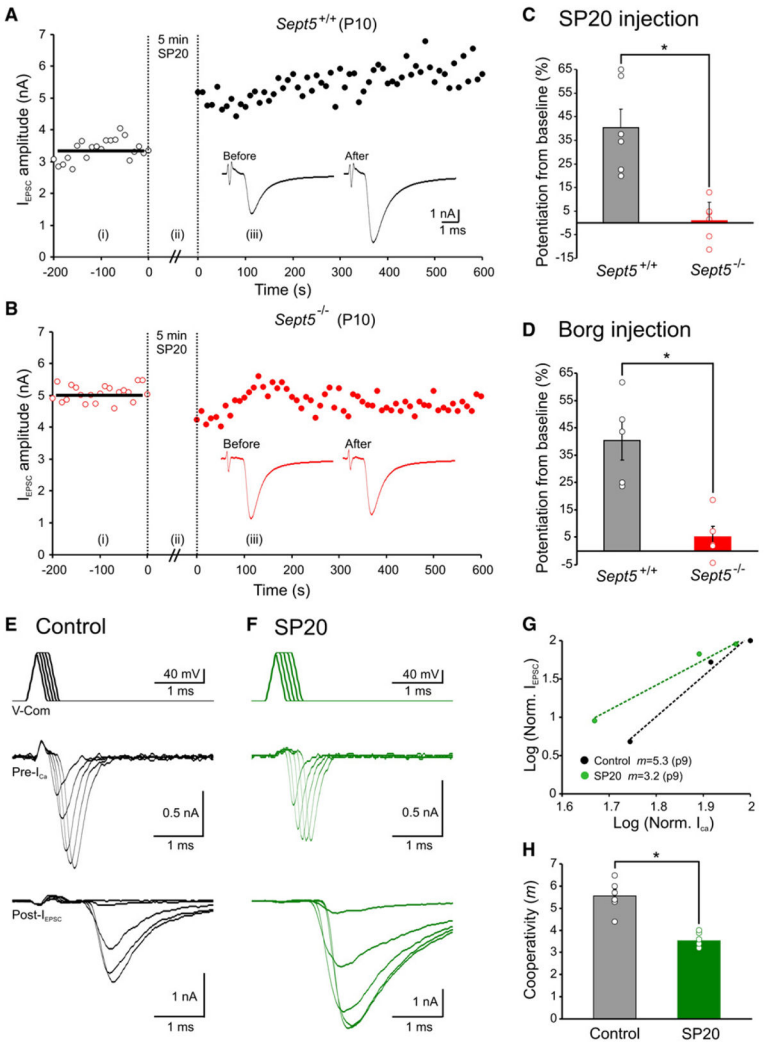

Figure 6. Acute Conversion of Microdomain to Nanodomain Coupling between VGCCs and SVs in Immature *Sept5*$^{+/+}$ Synapses

(A and B) Same experiments as EGTA injections in Figure 4, except that Sept5 antibody (SP20) or Borg peptide was introduced to immature *Sept5*$^{+/+}$ (A) and *Sept5*$^{-/-}$ (B) synapses.

(C and D) Summary plots of EPSC potentiation induced by SP20 (C) and Borg peptide (E).

(E and F) Paired presynaptic I_{Ca} and postsynaptic I_{EPSC} recordings, in response to the voltage-command protocol shown in top panels, from two immature *Sept5*$^{+/+}$ synapse preloaded with control and SP20 solutions.

(G) Log-Log plot of normalized I_{Ca} versus I_{EPSC} for the recordings in (E) and (F). Dashed lines are least-squares regression fits.

(H) Summary showing *m* values for immature *Sept5*$^{+/+}$ with or without SP20 antibody preloading.

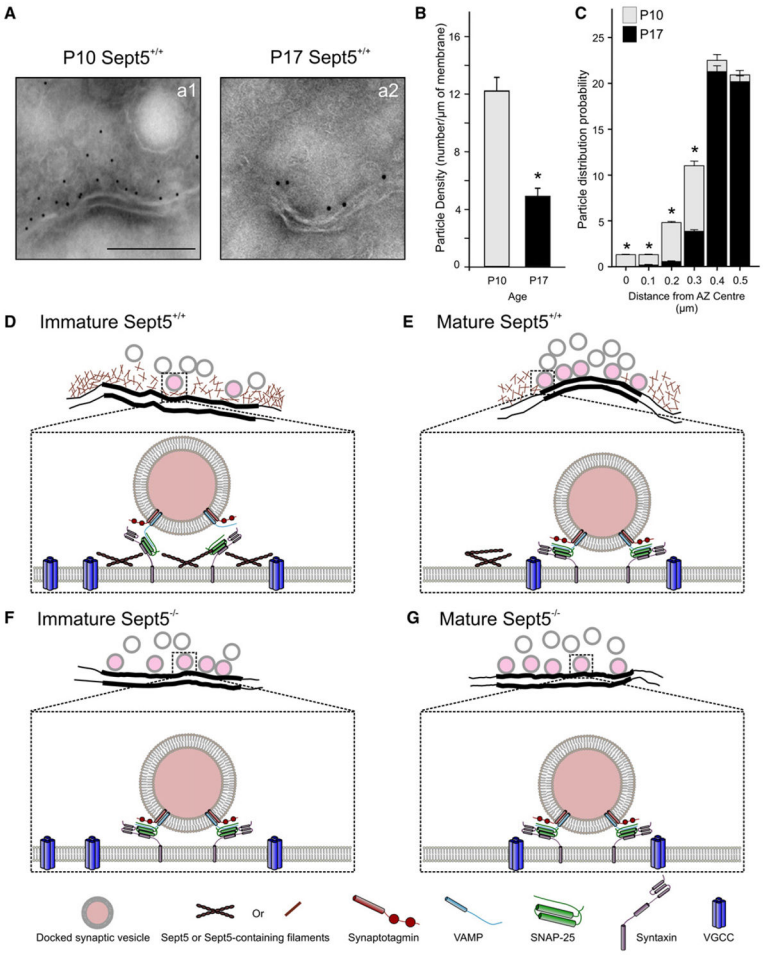

Figure 7. Subsynaptic Localization of Sept5 Filaments with Immunogold-EM and Proposed Roles of Sept5 in the Developing Calyx of Held Synapse

(A) Electron micrographs of the immature (left: P10) and mature (right: P17) calyx of Held synapse in ultrathin frozen sections labeled with Sept5 antibody (10 nm gold particles, SP20: 1:75 dilution), at which particle labeling were below the threshold of detection in control experiments from *Sept5*$^{-/-}$ tissues. The particle density (B) and the probability of particle distribution from the center of AZs (C) are summarized (n = 50 for each age group). Top panels in (D)–(G), are line drawings traced from EM images in Figure 2. Enlarged box depicts subsynaptic arrangements of release elements at the AZ.

(D) At immature terminals, Sept5 filaments bind to some SNAREs and form a mesh underneath SVs as a physical barrier for their docking onto AZs. This arrangement reduces the number of fully zippered SNAREs and keeps SVs vertically distant from AZs, raising the energy barrier for fusion. This spatial coupling (i.e., microdomain) displays high cooperativity (m = 5.5) and is highly sensitive to slow buffer EGTA. SP20 or Borg peptide breaks down Sept5 filaments and reduces the vertical distance and hence m value (3.5).

(E) At maturity, the expression of Sept5 filaments at AZs significantly decreases, resulting in more docked SVs, while VGCCs move closer to the release sites shortening lateral separation of VGCCs from SVs and forming nanodomain coupling modality with low cooperativity (m = 2.7) and little sensitivity to EGTA.

(F) In *Sept5*$^{-/-}$ synapses, SVs are tightly docked to AZs showing nanodomain-like coupling phenotypes including a reduced cooperativity (m = 3.3) and lack of sensitivity to EGTA. (G) With additional developmental regulation on the lateral placement of VGCCs in AZs, the cooperativity in mature *Sept5*$^{-/-}$ synapses further decreases (m = 3.0). Scale bar in A = 250 nm.